https://doi.org/10.1016/j.engstruct.2018.08.057

Cross-sectional behavior of cold-formed steel semi-oval hollow sections

Man-Tai Chen [a], Ben Young [b,*]

[a, b] *Department of Civil Engineering, The University of Hong Kong, Pokfulam Road, Hong Kong, China.*

Abstract

This paper presents an investigation on the material properties, residual stress distributions and cross-sectional behavior of cold-formed steel semi-oval hollow sections. Four cross-section series were included in the test program. The test specimens were cold-formed from hot-extruded seamless steel circular sections. Tensile coupon tests were conducted on coupon specimens extracted from three critical locations, namely the flat, curved and corner portions, of each cross-section as well as half of the cross-section of a representative section. Membrane and bending residual stresses distributions on the representative section were measured in both longitudinal and transverse directions. In addition, initial geometric imperfections were measured for each cross-section series and stub column tests were conducted to determine the average stress-strain relationship over the complete cross-section in the cold-worked state and to examine the cross-sectional behavior of cold-formed steel semi-oval hollow sections. Furthermore, a finite element model was developed and validated against the test results. With the verified finite element model, an extensive parametric study over a wide range of cross-section geometries was performed. The load-carrying capacities of stub columns obtained from experimental and numerical investigation were compared with the design strengths predicted by the Direct Strength Method using the design equations originally developed for open sections and the Continuous Strength Method with the design curves originally developed for traditional tubular sections. The comparison results show that the existing design methods provide conservative design strength predictions. In this study, modification on the Continuous Strength Method is proposed, which is shown to improve the accuracy of the design strength predictions in a reliable manner.

Keywords: Cold-formed; Residual stress; Semi-oval hollow sections; Stub column; Structural design.

---

* Corresponding author. Tel.: +852-2859-2674; fax: +852-2559-5337.
E-mail address: young@hku.hk (B. Young).

1. Introduction

The rapid development of steel manufacturing industry in recent decades has allowed the rise of more stringent requirements on the design of steel structures with regards of both structural efficiency and architectural appearance. Nowadays, the major challenges that the structural engineers are facing are not only restricted to the structural performance, but also closely related to the architectural perspective. With these requirements, metallurgical industry has sought to respond to the needs of the market and developed new forms of tubular profiles.

Without jeopardizing the structural efficiency and in the meantime retaining the aesthetic appearance, an innovative cross-section profile, semi-oval hollow section (SOHS), is recently developed by cold-forming. The semi-oval hollow section investigated in this study is composed of one semi-circular flange, one flat flange, and two flat web plates, as shown in Fig. 1a. It integrates the architectural elegance of circular hollow section with the structural advantages of rectangular hollow section associated with different flexural rigidities about the two principal axes. Despite of the merits of SOHS, no investigation has been conducted on this section yet, which limits the structural application of this section.

In this study, the material properties, residual stress distributions and cross-sectional behavior of cold-formed steel SOHS were investigated. The material properties for each cross-section series and the distribution of material strengths along half of the cross-section profile were measured and examined through tensile coupon tests. The average stress-strain relationships over the complete cross-section in the cold-worked state were also obtained from stub column tests. The initial local geometric imperfections of each cross-section series were measured. The distributions of membrane and bending residual stresses along half-section profile of a representative section were obtained in both longitudinal and transverse directions. Non-linear finite element (FE) model was developed to simulate the cold-formed steel SOHS stub column tests. The model was validated against the

experimental results and was further used in extensive parametric study to investigate the cross-sectional behavior of cold-formed steel SOHS with a wide range of cross-section geometries. The stub column strengths obtained from the experimental and numerical studies were compared with the design strengths predicted by the existing Direct Strength Method (DSM) [1] and Continuous Strength Method (CSM) [2-4]. Modification on the CSM is proposed in this study. The feasibility and reliability of the existing and modified design methods for SOHS were evaluated by means of reliability analysis.

2. Test specimens

Four series of SOHS were included in the experimental program with the cross-section geometry as defined using the nomenclature in Fig. 1a. The SOHS investigated in this study were fabricated by hot-extruded seamless steel circular hollow sections and then cold-formed into SOHS. Therefore, the SOHS are considered as cold-formed steel sections due to the involvement of the final cold-forming process. The nominal dimensions ($D\times B\times t$) of SOHS are 93×62×5.5, 107×68×6.5, 108×79×5.5 and 125×85×6.5, where D, B and t are the overall depth, overall width and thickness of the sections, respectively. The nominal cross-section aspect ratio (D/B) of the specimens varies slightly from 1.37 to 1.57.

3. Tensile coupon tests

3.1. General

Tensile coupon tests were conducted on coupon specimens extracted from three critical locations, namely the flat, curved and corner portions, of each cross-section as well as half of the cross-section of a representative section to determine the material properties of these sections and to investigate the distribution of material properties along cross-section profile. The material properties, including the Young's modulus (E), the 0.2% tensile proof stress ($\sigma_{0.2}$), ultimate tensile strength (σ_u) and tensile strain at fracture (ε_f), were measured.

3.2. Coupon specimens from critical locations

To characterize the material properties and examine the strength enhancement due to the cold-forming process for SOHS, twelve tensile coupon tests were conducted on four cross-section series of SOHS. For each cross-section series, tensile coupon specimens were machined from three critical locations, which are longitudinally along the flat web (TC1), the semi-circular flange (TC2) and the corner (TC3) of SOHS as shown in Fig. 1b. The flat coupon specimens were prepared in accordance with the American standard ASTM-E8M [5]. To examine the strength enhancement due to the cold-forming process of the specimens, curved coupon specimens extracted from the semi-circular flange and the corner region of the specimens were also prepared for testing. The nominal width of the curved coupon specimens for the gauge length of 25 mm was 4 mm. Two 7 mm diameter holes were drilled on both ends with the end clearance of 11.5 mm to avoid net section failure near the holes for the curved coupon specimens. The flat coupon specimens were 12.5 mm wide within 50 mm gauge length. Two strain gauges were adhered on both faces in the middle of the gauge length to determine the Young's modulus. The calibrated extensometer with 50 mm or 25 mm gauge length was mounted on the gauge length of the flat or curved coupon specimen, respectively, to capture the real-time extension of the specimens within the gauge length and then further converted to the longitudinal strain.

The tensile load was applied using displacement control with the loading rates of 0.05 mm/min and 0.4 mm/min for elastic and plastic range, respectively, as recommended by Huang and Young [6] for cold-formed carbon steel. All tensile coupon tests were performed using a 50 kN capacity MTS machine. The test rig adopted for flat coupon tests was different from that for curved coupon tests. The flat coupons were tested with both ends gripped with a pair of flat surface clamps as shown in Fig. 2a, whilst the curved coupons were tested between two pins installed in a pair of special loading rigs as shown in Fig. 2b to ensure that the load was applied through the centroid of the coupon specimens. Tests were paused for 100 seconds at three critical locations (i.e. near yield

stress, near the ultimate load as well as at post-ultimate stage) to allow for stress relaxation and to obtain the static stress-strain relationship. The coupon specimens were tested to fracture and these tests were considered to be successful only if the failure of specimen occurred within the gauge length.

The static material properties for coupon specimens extracted from three different critical locations could be further obtained from static stress-strain curves and are summarized in Table 1. The typical stress-strain histories of coupon specimens from three different critical locations in the SOHS with nominal dimensions ($D\times B\times t$) of 108×79×5.5 are depicted in Fig. 3.

It should be noted that among the three critical locations in the cross-section of SOHS, the minimum 0.2% proof stress and the minimum ultimate strength not necessarily take place in the flat coupon (TC1). They may take place in the coupon extracted from the semi-circular flange (TC2) instead in some cases. The reason for this phenomenon is illustrated as follows. The semi-oval sections in this study were cold-formed from hot-extruded seamless circular hollow sections with uniform material properties distribution. The magnitude of cold-forming effect is correlated to the amount of curvature change during the cold-forming process. The curvature difference between the hot-extruded seamless circular section and the flat portion of SOHS is not necessarily less than that between seamless circular section and semi-circular flange, hence, the minimum 0.2% proof stress and the minimum ultimate strength can occur in either flat web or semi-circular flange.

Significant strength enhancement and ductility reduction were observed at the corners of the sections. The coupon specimens from the corner regions possess higher 0.2% proof stress and ultimate strength by 15 to 39% and 9 to 15% than their counterparts from either the flat or semi-circular portion, whichever has lower material strengths, respectively. The ductility as represented by the fracture strain of material was significantly reduced by 20 to 35%.

3.3. Coupon tests in half-section

Coupon specimens were extracted from the half-section of a representative SOHS 125×85×6.5 and tested to examine the material properties distribution along cross-section profile. The SOHS in this study is seamless and the coupon specimens in half-section were extracted starting from the centerline of the section. To investigate the distribution of material properties in smaller interval, the distance between each coupon specimen was halved and the number of coupon specimens was doubled by extracting the coupon specimens from two successive segments in the same steel tube. A total of 18 coupon specimens was tested.

The preparation of coupon specimens was identical to those specimens described in the previous section for coupon specimens from flat, semi-circular and corner regions. It should be noted that standard coupon specimen with gauge length of 50 mm cannot be extracted in locations 3 and 5 as shown in Fig. 4, hence, the dimensions of sub-size coupon specimen specified in the American standard ASTM-E8M [5] were adopted. The nominal width of the sub-size coupon specimens for the gauge length of 25 mm was 6 mm. The test setup and procedure for flat and curve coupon specimens were identical to those described in the previous section.

The static material properties for coupon specimens extracted from the half-section of the representative SOHS 125×85×6.5 were obtained and are summarized in Table 2. The static material strengths including 0.2% proof stress and ultimate strength were plotted against the locations from which the coupon specimens were extracted to study the material strength distributions along half of the cross-section as shown in Fig. 4. The failed coupon specimens extracted from the half-section are shown in Fig. 5.

From the results, the significant strength enhancement at the corner region is evidenced by the possession of the highest 0.2% proof stress and the second highest ultimate strength at the corner region among all coupon specimens from half of the cross-section. The coupon specimen from

location 3 has the highest ultimate strength among all the specimens. This could be due to the location of the rollers in the cold-forming process. It should be noted that in general, coupon specimens from semi-circular region has a lower value of 0.2% proof stress than those from the flat web portion. This phenomenon was also found and explained in the previous section. In terms of ultimate strength, the difference between coupon specimens from flat web and semi-circular regions is very small.

4. Residual stress measurements

4.1. General

Residual stress of cold-formed section is the internal stress locked in the tubular section during cold-forming process. The residual stress distributions were measured on a representative SOHS with nominal cross-section dimensions of 125×85×6.5. The specimen was wire-cut to a total length of 260 mm, including the length of 250 mm for residual stress measurement in longitudinal direction and 10 mm wide ring for measurement in transverse direction. Strips with width of 10 mm were marked on half of the section in the longitudinal direction and a 10 mm transverse ring at one end of the specimen was also marked as shown in Fig. 6. The prepared strain gauges were adhered on the inner and outer surfaces of each longitudinal strip and the transverse ring, and were protected by waterproofing measures. A wire-cutting machine with an accuracy of 0.005 mm was used and coolant was applied to remove the heat generated during the cutting process. The 10 mm wide transverse ring was first cut off from the 260 mm long specimen, and was further cut open to release the stresses. The longitudinal residual strains were measured by the method of sectioning, and were further converted into residual stresses. Fig. 7 shows the SOHS in wire-cutting process. The readings of strain gauges and the room temperatures before and after cutting were recorded. Five sets of measurement were recorded for each strain gauge. The maximum and minimum values among five sets were removed and the average value of the remaining three sets was used in the calculation. The differences in strains obtained before and after cutting were converted to residual stresses by multiplying the measured Young's modulus at the corresponding locations. The bending

and membrane residual stresses (σ_b and σ_m) were calculated by Eqs. (1) and (2), respectively. The positive and negative values indicate the tensile and compressive residual stresses, respectively. Fig. 8 shows the sign convention of bending and membrane residual stresses and the corresponding deformations of the strip.

$$\sigma_b = -\left(\frac{\varepsilon_o - \varepsilon_i}{2}\right) \times E \tag{1}$$

$$\sigma_m = -\left(\frac{\varepsilon_o + \varepsilon_i}{2}\right) \times E \tag{2}$$

4.2. Longitudinal residual stresses

To investigate the distribution of residual stresses of SOHS, a total of 38 strain gauges was adhered on the longitudinal strips, 19 on outer surface and 19 on the corresponding locations on the inner surface. The room temperatures of the initial measurement and the measurement after cutting were both 21.5 °C. Fig. 9 shows the distribution of both bending and membrane residual stresses in longitudinal direction along half of the representative SOHS. The residual stresses were normalized to the lowest 0.2% proof stress in the section. Fig. 10 plots the normalized residual stresses against the location of strip. The results show that the bending residual stresses in 19 strips were all positive, indicating that the tensile and compressive bending residual stresses were locked in the section on the outer and inner surfaces, respectively. The magnitude of bending residual stress of each strip was higher than the corresponding membrane residual stress. The highest bending residual stress with the magnitude of 172.5% of the 0.2% proof stress of the material was observed in the strip next to the corner. This concurred with the severe bending of strip at that location after sectioning as shown in Fig. 11. The maximum membrane residual stress with the magnitude of 30.7% of the 0.2% proof stress of the material was much less significant compared with the bending residual stress.

4.3. Transverse residual stresses

Besides the longitudinal residual stresses, the transverse residual stresses were also measured. A total of 28 strain gauges was adhered on the 10 mm wide transverse ring, 14 on outer surface and 14 on the corresponding locations on the inner surface. A 10mm wide transverse ring was cut out from the end of 260 mm long specimen. Another cut was applied to the flat web region of the transverse ring with no transverse strain gauge adhered to release the transverse residual stresses. Since the transverse ring did not visibly open after cutting, an additional cut was applied to ensure the transverse residual stresses fully released. From the transverse ring as shown in Fig. 12, the section was hardly deformed after cutting. The room temperatures of the initial measurement and the measurement after cutting were both 21.5°C. Fig. 13 depicts the distribution of both bending and membrane residual stresses in transverse direction along half of the cross-section. The residual stresses were normalized to the lowest 0.2% proof stress and the normalized residual stresses are plotted against the location of measurement as shown in Fig. 14. Comparing with the bending residual stresses in longitudinal direction, the magnitudes of bending residual stresses in transverse direction were much smaller. The magnitudes of maximum bending and membrane residual stresses were 50.9% and 31.1% of the 0.2% proof stress of the material, respectively.

5. Geometric imperfection measurements

Prior to testing, the initial local geometric imperfections were measured for each SOHS stub columns. For each of the four series of sections, all test specimens were cut and machined from the same batch of tubes. Therefore, it is reasonable to measure the initial local geometric imperfections on the stub columns only but not specifically on each test specimen, and use the measured results to represent the initial local imperfections induced in the forming process for each section.

Fig. 15 shows the setup and the Linear Variable Displacement Transducers (LVDTs) arrangement of the measurement as well as the sign convention of measured local imperfection. The specimens were placed on a measurement platform and a set of three LVDTs with an accuracy

of 0.001 mm was affixed to the head of a milling machine. For the three flat faces of the section, i.e. Faces A, C and D as shown in Fig. 15a, the local geometric imperfections were assumed to be zero at the corners and the maximum local plate imperfection was anticipated to occur at the mid-portion of the webs and flange. In this case, three LVDTs were positioned on the specimen with two located near the corners of the section and one at the mid-portion of the flat plate as shown in Fig. 15. Measurement was taken at a 5 mm interval along the specimen length. For the purpose of eliminating the possible local imperfection induced by cold sawing of the specimen, measurements were started and terminated 30 mm away from the ends of the specimens. Such procedure was repeated at each of the three flat faces of the five specimens. The local plate imperfections of flat faces were taken to be the deviation between the measurements at the mid-portion and a straight datum line connecting the measurements at the corners of the section as shown in Fig. 15a. For the semi-circular face (face B) of the section, one LVDT was employed to inspect the concavity/convexity along the specimen length at the tip of semi-circular portion. Similarly, the measurement was taken longitudinally at 5 mm interval. The measurement was corrected with reference to the datum taken as a straight line connecting the start and end measurement points.

Fig. 16 depicts the typical measured local geometric imperfection profile along the four faces for specimen 93×62×5.5-SCL235. The maximum local geometric imperfections ω_l inherent in each of the five stub column specimens are reported in Table 3.

6. Stub column tests

Five fixed-ended stub column tests were included in the test program. All the SOHS stub columns are labeled such that the nominal cross-section geometry, the specimen type and the specimen length can be identified. The specimen label consists of two parts, which are separated by a hyphen. The first part of the label identifies the nominal cross-section geometry of the test

specimen. The letters SC in the second part of the specimen label indicate a stub column. The following letter L together with the number designate the specimen length, whereas the symbol # denotes a repeated test. The measured specimen dimensions are reported in Table 3, where r_o and r_i are the external and internal corner radii, respectively, and L is the specimen length.

Stub column tests were conducted for each cold-formed steel SOHS to assess the average stress-strain relationships, load-carrying capacities and load-end shortening histories of the complete cross-sections in the cold-worked state between fixed ends under uniform axial compression. The nominal stub column length of 2-4 times the larger dimension of cross-section [7-12] was deemed to be sufficiently long to provide a valid measure of the stress-strain relationship and load-end shortening history as averaged over the cross-section with consideration of representative distribution of geometric imperfections and residual stresses induced in the cold-forming process, but suitably short to avoid flexural buckling in the elastic or plastic range. In this study, the nominal length of the stub columns was taken to be 2.5 times the overall depth of the cross-section. The ends of specimens were milled flat to achieve the uniform loading over the cross-section and accurate seating in the testing machine. A pair of special clamping devices with a height of 25 mm was installed near the two ends of specimens with a small gap of around 3 mm between the clamping devices and the adjacent bearing plates in order to avoid premature end failure.

The schematic illustration of the test setup and a view of experimental arrangement of stub column test are shown in Fig. 17. The test setup consisted of four LVDTs to determine the average end shortening, three strain gauges attached on the mid-height of specimen near the two corners and at the tip of semi-circular portion to measure the axial strain and one additional strain gauge to detect the initiation of local bucking, if any, as depicted in Fig. 17. Similar test arrangements have been adopted by various researchers [7, 10, 13-17]. The stub columns were compressed in an INSTRON hydraulic testing machine, at a constant speed of 0.5 mm/min. The applied displacement

was paused for 100 seconds near the ultimate load. Therefore, static stress-strain responses and load-end shortening histories can be obtained and are depicted in Fig. 18. From the average stress-strain responses obtained from the stub column tests, the Young's modulus (E_{SC}), 0.2% proof stress ($\sigma_{0.2\text{-}SC}$) and ultimate strength ($\sigma_{u\text{-}SC}$) were obtained as reported in Table 4. The obtained results were further compared with the material properties of tensile coupon specimens with the lowest 0.2% proof stress as shown in Table 4. From the comparison, the 0.2% proof stress and the ultimate strength obtained from stub column tests are larger than those from tensile coupon tests. This demonstrates the full utilization of cross-section axial capacity.

The ultimate load-carrying capacities and the corresponding end shortenings are summarized in Table 5. The effective length (L_e) of the stub column was taken as half of the specimen length. No elastic local buckling was observed during the tests. The squash load (P_y^) of the stub column specimen, which was calculated as the sum of the 0.2% proof stresses at the flat, semi-circular and corner portions multiply by their corresponding cross-section areas, was compared with its ultimate load-carrying capacity. It is shown in Table 5 that the ratio of ultimate strength to squash load for all SOHS stub column specimens is greater than unity, which indicates that none of the SOHS stub columns failed by elastic local buckling, hence the SOHS investigated herein are considered as non-slender sections. Photo of failed stub column specimens is shown in Fig. 19.

7. Numerical investigation

7.1. Finite element model and validation

In the validation of finite element model, the measured cross-section geometries as reported in Table 3, the measured Young's modulus and the converted true plastic stress-strain response were used. The measured full length of actual specimen was modeled. The fixed-ended boundary conditions of stub columns were simulated by restraining the specimen ends against all degrees of freedom, except for the longitudinal displacement at one loading end. The compressive load was

applied by specifying the axial displacement using a static RIKS step. The nonlinear geometric parameter (*NLGEOM) was enabled to allow for large displacement analysis.

The commonly used four-node shell element with reduced integration (S4R) was used in the finite element model. The value of (B+D)/30 was taken as the mesh size in the flat and semi-circular portions, whilst finer mesh was used for corner regions. The mesh was assigned uniformly along longitudinal direction of the stub column specimen.

The residual stresses in longitudinal direction usually have more influence on the behavior of the structural steel members. The maximum bending and membrane residual stresses are 172.5% and 30.7% of the 0.2% proof stress of the material. In terms of the inclusion of residual stress, the embedded bending residual stress in longitudinal direction with a significant magnitude of 172.5% of 0.2% proof stress has been inherently incorporated into the measured material properties obtained from coupon tests. It is rational not to explicitly incorporate the membrane residual stress into the finite element model since its magnitude and the corresponding influence on the structural responses are much lesser compared to those for bending residual stress [10, 18-20]. To further verify the unnecessity of explicit inclusion of residual stress, the measured membrane residual stress distribution for SOHS with nominal dimensions of 125×85×6.5 was incorporated explicitly in the finite element model, the results of which were compared with the results obtained from the model without the inclusion of membrane residual stresses. Fig. 20 shows the comparison of load-end shortening responses obtained from the stub column models with and without the inclusion of membrane residual stresses. The comparison result supports that the influence of residual stresses on the structural response of cold-formed steel SOHS is negligible. For simplification, bending and membrane residual stresses were not explicitly included in the finite element model.

In general, the material strength in the corner region was significantly enhanced during the cold-forming process of the SOHS. The cold-forming effect should also be considered in the modeling process. The strength enhancement was not restricted to the corner region, but extended to a certain distance away from the corner. In this study, sensitivity analysis on the corner region extension of SOHS was conducted to determine the length of extension. The corner was extended by t, $2t$ and $2.5t$ in the sensitivity analysis as shown in Fig. 21. Table 6 summarizes the comparison results of the sensitivity analysis and shows that different corner extensions provide similar predictions with only 1% on average. The value of corner region extension was taken to be $2t$ in the numerical model, which echoed with the commonly adopted value suggested by previous researchers [10, 20-22].

The lowest elastic local buckling mode shape obtained by eigenvalue analysis was taken as the initial local geometric imperfection profile of the stub column, and the buckling mode shape was amplified by a certain magnitude of imperfection. Although the measured average value of initial local imperfections was around $t/16$, sensitivity analysis was performed to determine the proper magnitude of imperfection incorporated in the model. Three imperfection amplitudes, expressed as the fractions of section thickness ($t/16$, $t/50$ and $t/100$), were included in the sensitivity analysis, as shown in Table 6. The magnitude of local imperfection of $t/50$ was used in the modeling, which was shown to provide better replication to SOHS stub column tests as evident by the mean value of test-to-FE strength ratio close to unity and the possession of the smallest value of COV.

With the aforementioned modeling parameters and assumptions, the finite element model of stub columns was developed and validated against 5 SOHS stub column tests. The second last column of Table 5 shows the validation results for the final model. The finite element model can successfully replicate the axial load-carrying capacities of the cold-formed steel SOHS stub column specimens as evidenced by the mean value and COV of the test-to-FE strength ratio of 1.00 and 0.023, respectively. The comparison of load-end shortening responses obtained from the test and

finite element model for typical SOHS stub column specimen are presented in Fig. 22. The failure mode can also be captured in the finite element model as shown in Fig .23.

7.2. Parametric study

Material properties obtained from the three critical locations of SOHS 107×68×6.5 were used in the finite element analysis. The validated finite element model for stub column was used to perform extensive parametric study on cold-formed steel SOHS under uniform compression. Finite element analysis on a total of 40 stub column specimens was conducted. Extensive range of cross-section dimensions and slenderness was designed for the parametric study. The aspect ratio (D/B) of the SOHS varies from 1.25 to 2.50. The overall depth of the section varies from 140 to 450 mm. The thickness of the section was designed to cover a spectrum of slenderness ratio from stocky to slender sections. The length of stub column was taken to be 2.5 times the overall depth of the SOHS. The results obtained from the numerical study are summarized in Table 7. The results from numerical study together with the experimental results were used for the assessment of existing design methods and modified design rule.

8. Comparison of stub column strengths with design strengths

8.1. General

The current international design specifications for tubular members only cover the structural design of traditional cross-section types, such as square, rectangular and circular hollow sections, but not the newly emerged SOHS. Therefore, the SOHS stub column strengths obtained from experimental and numerical investigation were compared with the nominal strengths (unfactored design strengths) predicted by the Direct Strength Method using the design equations calibrated by open sections and the Continuous Strength Method with the design curves originally developed for traditional tubular sections. The material properties obtained from coupon tests in the location with lowest 0.2% proof stress were used in nominal strength calculation for conservative predictions. The feasibility of current and modified design methods was evaluated through reliability analysis as

detailed in the North American Specification AISI-S100 [1]. The values of resistance factor (ϕ) are 0.85 and 1.0 for the Direct Strength Method and the Continuous Strength Method, respectively. Together with the calibration coefficient determined by the load combination specified in the North American Specification AISI-S100 [1] and the European Code EN1993-1-1 [23] as well as the statistical parameters as specified in the North American Specification AISI-S100 [1], the reliability indices of different design methods for strength predictions of cold-formed steel SOHS stub columns are therefore obtained as shown in Table 8. The design method is considered to be reliable only if the resulted reliability index (β) exceeds the lower limit of 2.5.

8.2. Direct Strength Method

The finite strip method used by the Direct Strength Method is applicable to arbitrary cross-sections for critical elastic buckling stress predictions. However, since the DSM design equations were originally calibrated by open sections with plate elements, the applicability and reliability of the DSM for the design strength predictions of the cold-formed steel SOHS stub columns are questionable and were therefore evaluated in this study.

The Direct Strength Method for compressive member design is detailed in Chapter E of the AISI-S100 [1]. The nominal axial strength was determined by the minimum of the nominal axial strengths for flexural buckling as well as local buckling and distortional buckling. For SOHS stub columns, neither global buckling nor distortional buckling was observed. The nominal axial strength predicted by the DSM (P_{DSM}) was therefore taken as the nominal axial strength of SOHS for local buckling. To determine the nominal axial strength for local buckling, the critical elastic local buckling load was obtained from CUFSM program using the finite strip method [24] with a 1 mm half-wave length interval and was subsequently substituted into the DSM design equations.

The results obtained from experimental and numerical investigation in this study were compared with the DSM predictions as shown in Table 8 and Fig. 24. The mean value of P_u/P_{DSM} is

1.14 with the corresponding COV of 0.123. The resulted reliability index is 2.99 for the resistance factor of 0.85. The results indicate that the existing DSM as detailed in the AISI-S100 [1] provides conservative and reliable design strength predictions for cold-formed steel SOHS stub columns.

8.3. Continuous Strength Method

The deformation-based design method, Continuous Strength Method [2-4, 25], considers the strain hardening of the metallic material and element interaction of the section. The cross-section classification and effective area calculation are not needed in the design strength prediction. In the CSM prediction, different based curves should be adopted for different section types to define the strain capacity of the section. Currently, the base curve is only available for the commonly used tubular sections, such as square, rectangular and circular hollow sections, but not for the newly developed semi-oval hollow sections investigated in this study. In terms of material model, the material model for cold-formed structural steel section proposed by Buchanan *et al.* [4] was adopted herein for cold-formed steel SOHS. Since the semi-oval hollow section comprises three flat plates and one semi-circular plate, the behavior of SOHS might lie between that of rectangular hollow section (RHS) and circular hollow section (CHS). The applicability of the RHS and CHS approaches of the CSM for the design strength predictions of cold-formed steel SOHS stub columns was evaluated.

The results obtained from the tests and parametric study were compared with the nominal axial strengths predicted by the two approaches of the CSM as shown in Table 8, Figs. 25 and 26. The mean values of $P_u/P_{CSM,RHS}$ and $P_u/P_{CSM,CHS}$ are 1.10 and 1.14 with the corresponding COV values of 0.040 and 0.189 for design strength predictions by the RHS and CHS approaches of the CSM, respectively. With the resistance factor of 1.0, the resulted reliability indices are 2.37 and 1.96 for RHS and CHS approaches of the CSM, respectively. From the results, it is found that the RHS and CHS approaches of the CSM provide conservative but unreliable predictions for

cold-formed steel SOHS stub columns. Modification on the Continuous Strength Method for cold-formed steel SOHS stub columns is required.

8.4. Modified Continuous Strength Method

The base curves of RHS [2] and CHS [4] as well as the modified base curve for SOHS are shown in Fig. 27. From the comparison with design strength predictions by the existing CSM for cold-formed steel SOHS stub columns, it can be concluded that the two approaches of the CSM were conservative but unreliable. Modified base curve is proposed for the newly developed SOHS as shown in Eq. (3) for the existing CSM.

$$\begin{cases} \left(\frac{\varepsilon_{csm}}{\varepsilon_y}\right)_{SOHS} = \frac{0.555}{\lambda_{CSM}^{3.9}} \le \text{lesser}\left(15, \frac{0.4\varepsilon_u}{\varepsilon_y}\right) & \text{for } \lambda_{CSM} \le 0.86 \\ \left(\frac{\varepsilon_{csm}}{\varepsilon_y}\right)_{SOHS} = \left(1 - \frac{0.09}{\lambda_{CSM}^{0.7}}\right)\frac{1}{\lambda_{CSM}^{0.7}} & \text{for } \lambda_{CSM} > 0.86 \end{cases} \quad (3)$$

The applicability of the modified CSM for SOHS was assessed by comparing the experimental and numerical results obtained from this study with the design predictions by the modified CSM as shown in Table 8 and Fig. 28. The mean P_u/P_{CSM}* is 1.01 and the corresponding COV is 0.073. The accuracy of nominal axial strength prediction is improved by adopting the modified CSM. The resulted reliability index is 2.61 with the proposed resistance factor of 0.85, indicating that the modified CSM is reliable. Local imperfection with the magnitude of t/50 is considered in the modified CSM.

9. Conclusions

The material properties, residual stress distributions and cross-sectional behavior of cold-formed steel semi-oval hollow sections have been investigated and described. Initial local geometric imperfections for each cross-section series were measured. Tensile coupon tests were

conducted on coupon specimens extracted from three critical locations as well as half of the cross-section of a representative section. The membrane and bending residual stresses were measured and plotted along half-section profile. Stub column tests were carried out to determine the average stress-strain relationship over the cross-section and to investigate the cross-sectional behavior of cold-formed steel semi-oval hollow sections. Finite element model was developed to simulate the stub column tests. A parametric study with a wide range of cross-section geometries was performed using the validated model. The experimental and numerical results were compared with the design strengths predicted by the Direct Strength Method and the Continuous Strength Method. It is shown that the design strength predictions by existing design methods are conservative. Therefore, modification on the Continuous Strength Method is proposed in this study. The modified Continuous Strength Method with the proposed resistance factor of 0.85 is able to provide accurate design strength predictions for cold-formed steel semi-oval hollow section stub columns in a reliable manner.

Acknowledgements

The authors are grateful to Shenyang Dongyang Special Section Tube for supplying the test specimens. The authors are also thankful to Miss Hoi-Kiu CHAN and Miss Ning-Yan CHAN for their assistance in the experimental program as part of their final year undergraduate research projects at The University of Hong Kong. The research work described in this paper was supported by a grant from the Research Grants Council of the Hong Kong Special Administrative Region, China (Project No. 17267416).

References

[1] AISI-S100 2016. North American Specification for the design of cold-formed steel structural members. *AISI S100-16.* Washington,D.C., USA: American Iron and Steel Institute.

[2] AISC 2013. Structural Stainless Steel. *AISC Design Guide 30.* American Institute of Steel

Construction.

[3] Gardner L. The continuous strength method. Structures and Buildings 2008;161(3):127-133.

[4] Buchanan C, Gardner L, Liew A. The continuous strength method for the design of circular hollow sections. Journal of Constructional Steel Research 2016;118:207-216.

[5] ASTM-E8M 2016. Standard Test Methods for Tension Testing of Metallic Materials. *ASTM E8M-16.* West Conshohocken, PA, USA.

[6] Huang Y, Young B. The art of coupon tests. Journal of Constructional Steel Research 2014;96:159-175.

[7] Chan TM, Gardner L. Compressive resistance of hot-rolled elliptical hollow sections. Engineering Structures 2008;30(2):522-532.

[8] Lai MH, Ho JCM. Confinement effect of ring-confined concrete-filled-steel-tube columns under uni-axial load. Engineering Structures 2014;67:123-141.

[9] Lai MH, Ho JCM. Axial strengthening of thin-walled concrete-filled-steel-tube columns by circular steel jackets. Thin-Walled Structures 2015;97:11-21.

[10] Ma JL, Chan TM, Young B. Experimental investigation on stub-column behavior of cold-formed high-strength steel tubular sections. Journal of Structural Engineering 2015;142(5):04015174.

[11] Ren QX, Han LH, Lam D, Hou C. Experiments on special-shaped CFST stub columns under axial compression. Journal of Constructional Steel Research 2014;98:123-133.

[12] Wang J, Afshan S, Schillo N, Theofanous M, Feldmann M, Gardner L. Material properties and compressive local buckling response of high strength steel square and rectangular hollow sections. Engineering Structures 2017;130:297-315.

[13] Chan TM, Huai YM, Wang W. Experimental investigation on lightweight concrete-filled cold-formed elliptical hollow section stub columns. Journal of Constructional Steel Research 2015;115:434-444.

[14] Galambos TV 1998. *Guide to stability design criteria for metal structures*, John Wiley & Sons.

[15] Huang Y, Young B. Material properties of cold-formed lean duplex stainless steel sections.

Thin-walled structures 2012;54:72-81.

[16] Young B, Hartono W. Compression tests of stainless steel tubular members. Journal of Structural Engineering 2002;128(6):754-761.

[17] Zhu JH, Young B. Tests and design of aluminum alloy compression members. Journal of structural engineering 2006;132(7):1096-1107.

[18] Huang Y, Young B. Experimental and numerical investigation of cold-formed lean duplex stainless steel flexural members. Thin-Walled Structures 2013;73:216-228.

[19] Huang Y, Young B. Structural performance of cold-formed lean duplex stainless steel columns. Thin-Walled Structures 2014;83:59-69.

[20] Zhao O, Rossi B, Gardner L, Young B. Behaviour of structural stainless steel cross-sections under combined loading–Part II: Numerical modelling and design approach. Engineering Structures 2015;89:247-259.

[21] Gardner L, Nethercot DA. Numerical modeling of stainless steel structural components - a consistent approach. Journal of Structural Engineering 2004;130(10):1586-1601.

[22] Ma JL, Chan TM, Young B. Design of cold-formed high strength steel tubular beams. Engineering Structures 2017;151:432-443.

[23] EN1993-1-1 2005. Design of steel structures–Part 1.1: General rules and rules for buildings. *EN 1993-1-1:2005.* Brussels, Belgium: European Committee for Standardization.

[24] Schafer BW, Ádány S. Buckling analysis of cold-formed steel members using CUFSM: conventional and constrained finite strip methods. In: Eighteenth International Specialty Conference on Cold-Formed Steel Structures, Orlando, FL, USA; 2006. p. 39-54.

[25] Yun X, Gardner L, Boissonnade N. The continuous strength method for the design of hot-rolled steel cross-sections. Engineering Structures 2018;157:179-191.

Nomenclature

B	Overall width of the section
CHS	Circular hollow section

COV	Coefficient of variation
CSM	Continuous strength method
D	Overall depth of the section
DSM	Direct strength method
E	Young's modulus
E_{SC}	Young's modulus obtained from stub column test
FE	Finite element
L	Specimen length
L_e	Effective length
P_{CSM}*	Nominal axial strength predicted by the modified Continuous Strength Method
$P_{CSM,CHS}$	Nominal axial strength predicted by the CHS approach in the Continuous Strength Method
$P_{CSM,RHS}$	Nominal axial strength predicted by the RHS approach in the Continuous Strength Method
P_{DSM}	Nominal axial strength predicted by the Direct Strength Method
P_{Exp}	Experimental loading capacity
P_{FE}	Finite element loading capacity
P_u	Ultimate axial loading capacity
P_y^	Squash load of cross-section considering the cold-forming enhancement
RHS	Rectangular hollow section
r_i	Inner corner radius of the section
r_o	Outer corner radius of the section
SOHS	Semi-oval hollow section
t	Thickness of the section
TC	Tensile coupon specimen
β	Reliability index
δ_u	End shortening at ultimate load

ε_{csm}	Limiting strain for the cross-section
ε_f	Tensile strain at fracture
ε_i	Residual strain on inner surface
ε_o	Residual strain on outer surface
ε_u	Ultimate strain
ε_y	Yield strain
ϕ	Resistance factor
λ_{CSM}	Cross-section slenderness in the Continuous Strength Method
σ_b	Bending residual stress
σ_m	Membrane residual stress
σ_u	Static ultimate tensile strength of material
$\sigma_{u\text{-}SC}$	Static ultimate tensile strength of material obtained from stub column test
$\sigma_{u\text{-}TC}$	Static ultimate tensile strength of material obtained from tensile coupon test
$\sigma_{0.2}$	Static 0.2% tensile proof stress of material
$\sigma_{0.2\text{-}SC}$	Static 0.2% tensile proof stress of material obtained from stub column test
$\sigma_{0.2\text{-}TC}$	Static 0.2% tensile proof stress of material obtained from tensile coupon test
ω_l	Initial local geometric imperfection

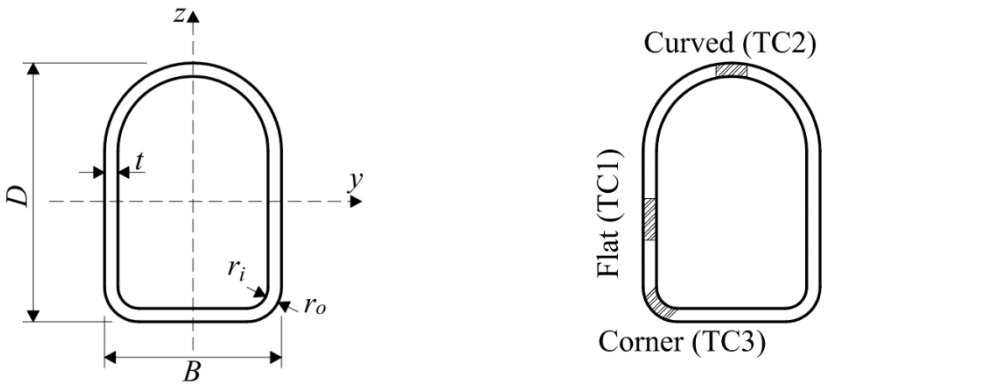

(a) Cross-section geometry (b) Locations of tensile coupon specimens

Figure 1. Cross-section of SOHS

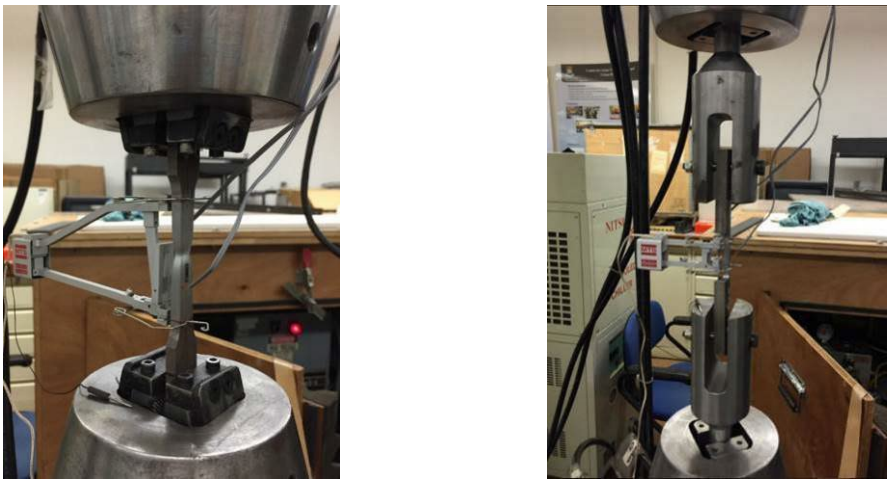

(a) Flat coupon test (b) Curved coupon test

Figure 2. Setup of tensile coupon tests of SOHS

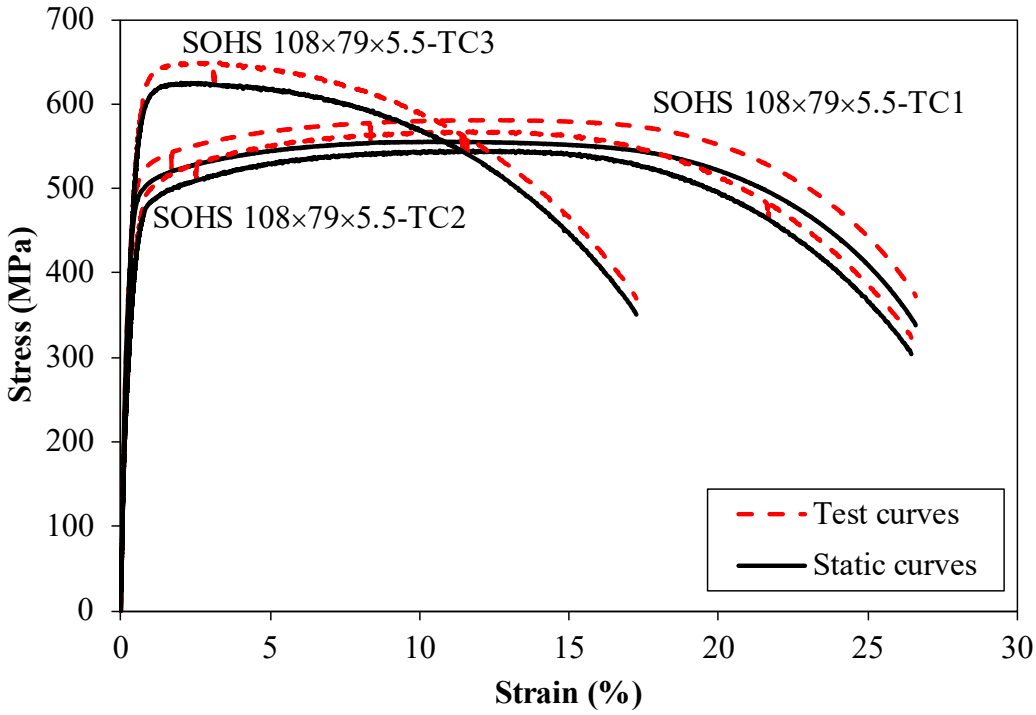

Figure 3. Test and static stress-strain histories of SOHS 108×79×5.5

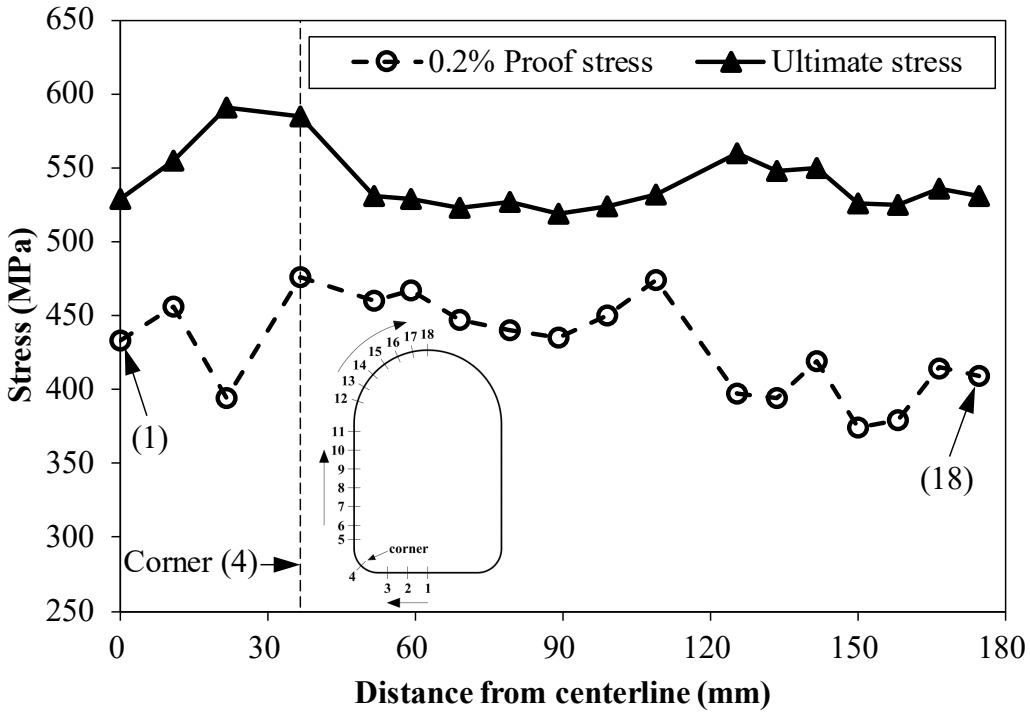

Figure 4. Measured material strengths distribution in SOHS 125×85×6.5

Figure 5. Failed coupon specimens from the half-section of SOHS 125×85×6.5

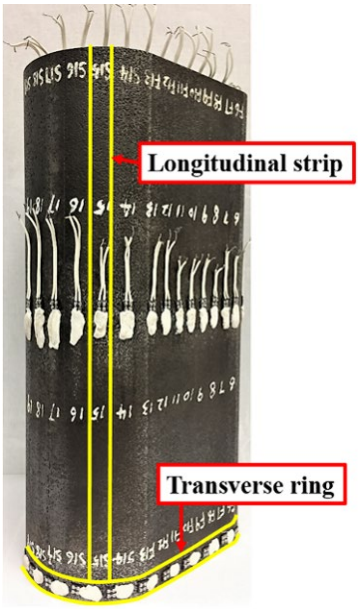

Figure 6. Specimen for residual stress measurements of SOHS 125×85×6.5

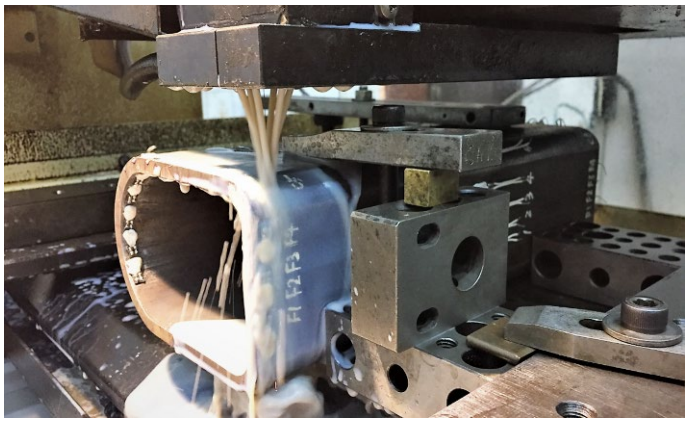

Figure 7. SOHS 125×85×6.5 in wire-cutting process

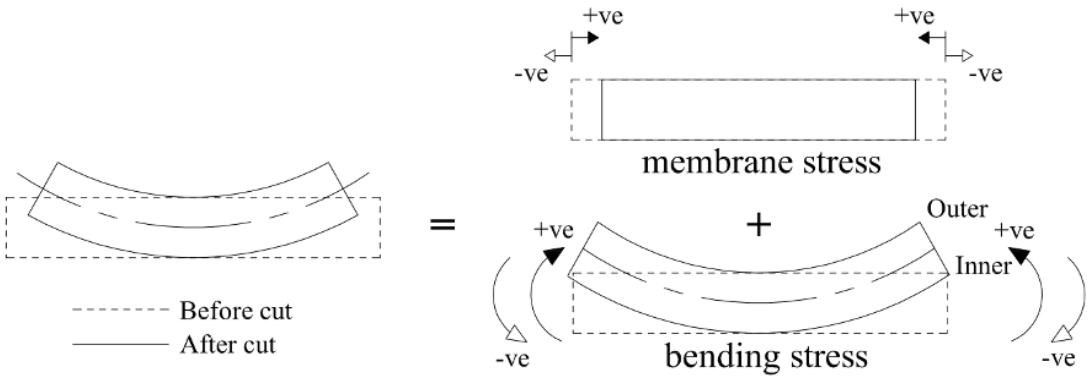

Figure 8. The sign convention for bending and membrane residual stresses

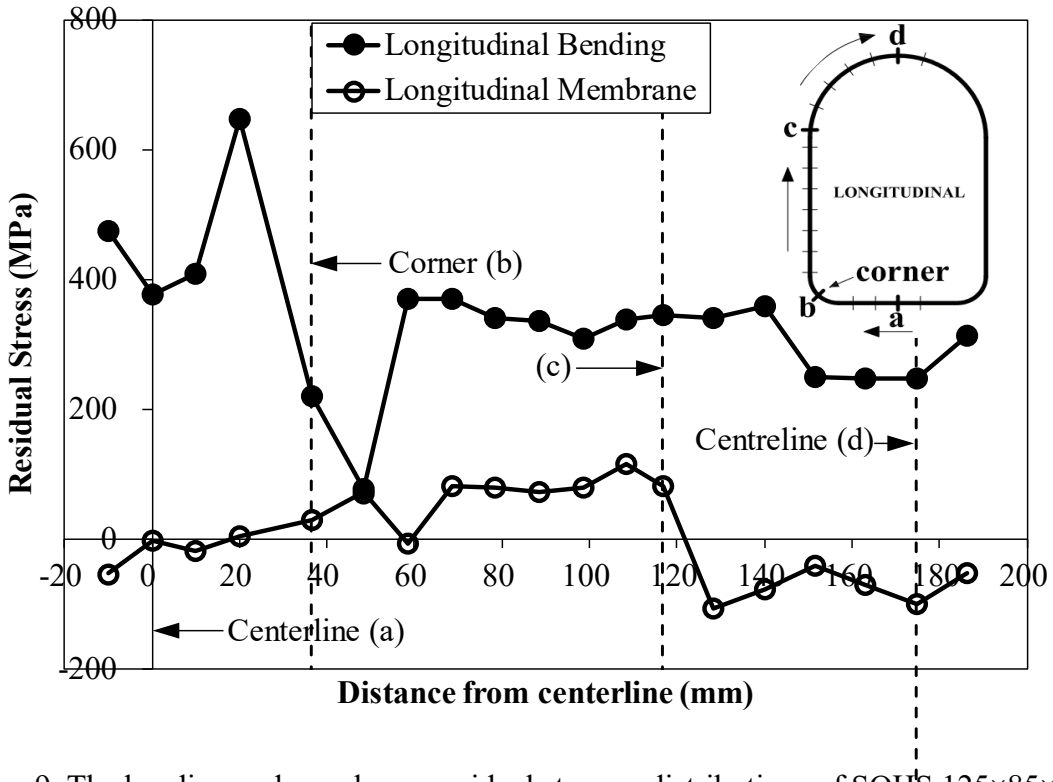

Figure 9. The bending and membrane residual stresses distributions of SOHS 125×85×6.5 in longitudinal direction

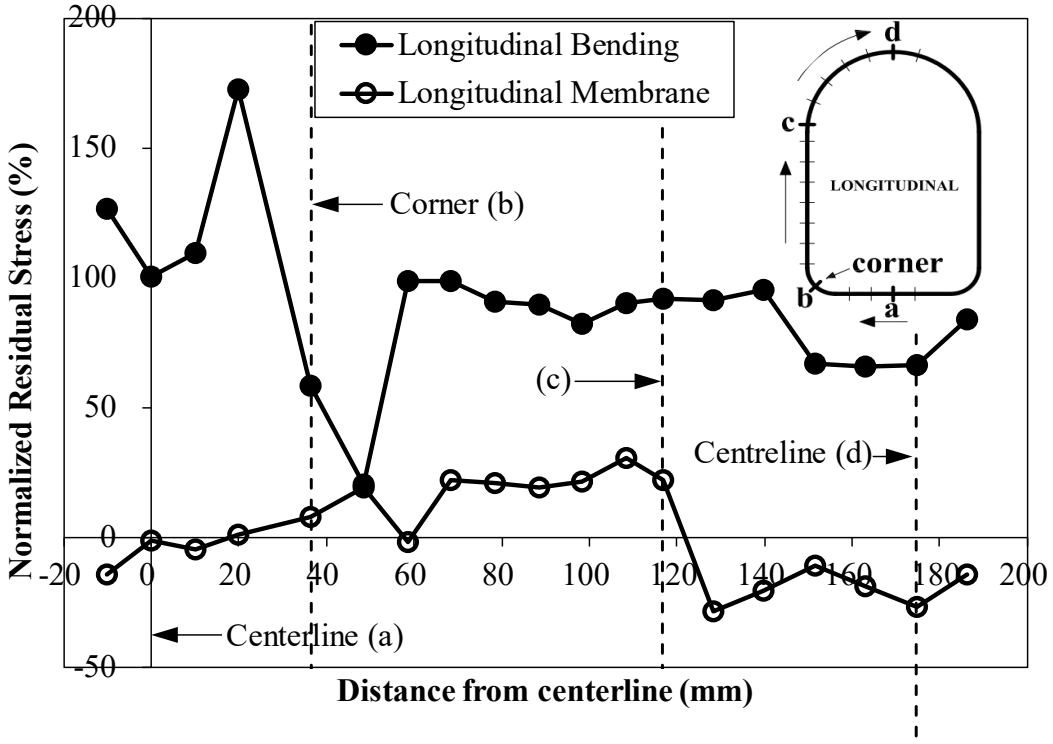

Figure 10. The normalized residual stresses distributions of SOHS 125×85×6.5 in longitudinal direction

Figure 11. Deformed longitudinal strips of SOHS 125×85×6.5 after cutting

Figure 12. Deformed transverse ring of SOHS 125×85×6.5 after cutting

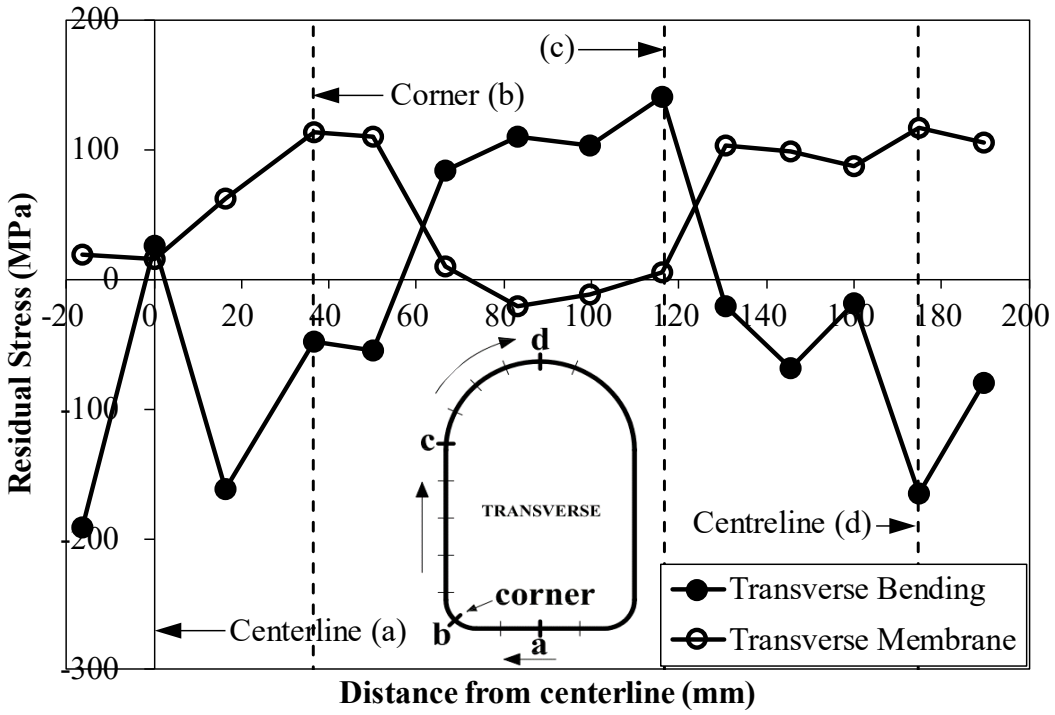

Figure 13. The bending and membrane residual stresses distributions of SOHS 125×85×6.5 in transverse direction

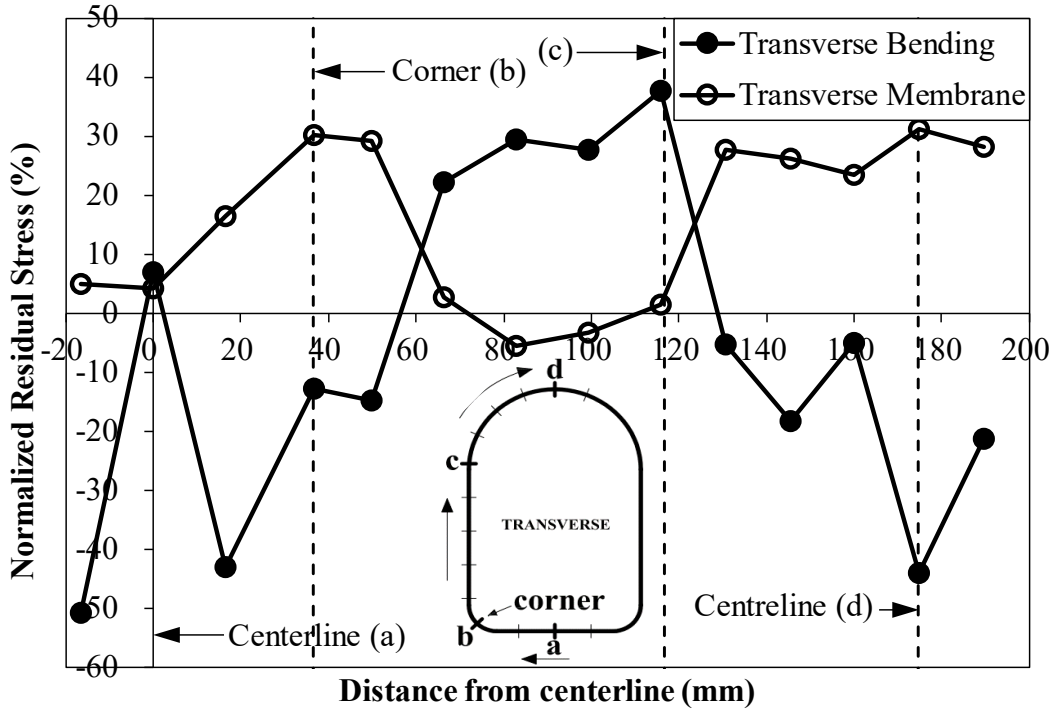

Figure 14. The normalized residual stresses distributions of SOHS 125×85×6.5 in transverse direction

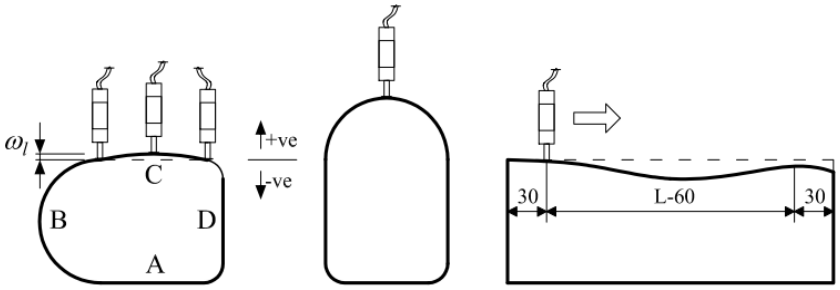

(a) Schematic view

(b) Experimental arrangement

Figure 15. Setup of local geometric imperfection measurements for SOHS

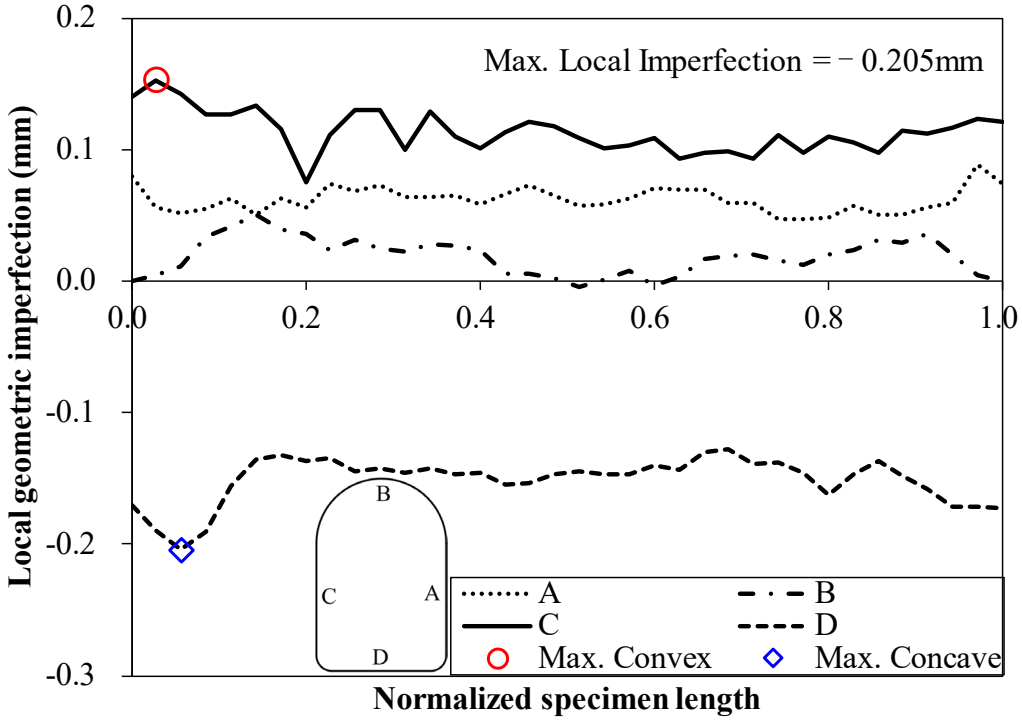

Figure 16. The distributions of local geometric imperfections along the length of SOHS stub column specimen 93×62×5.5-SCL235

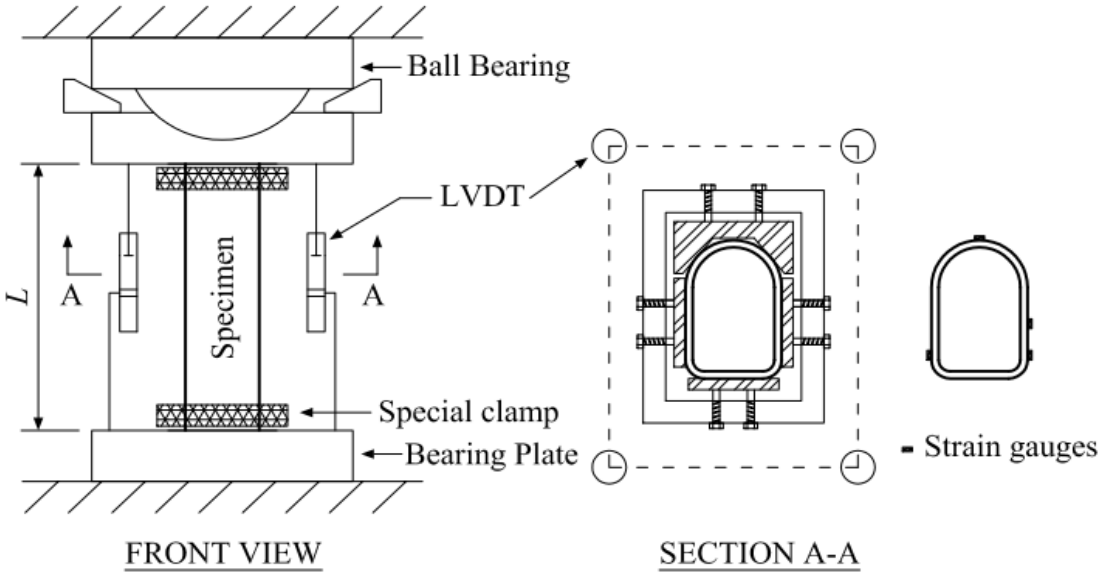

(a) Schematic view

(b) Experimental arrangement

Figure 17. Setup of SOHS fixed-ended stub column test

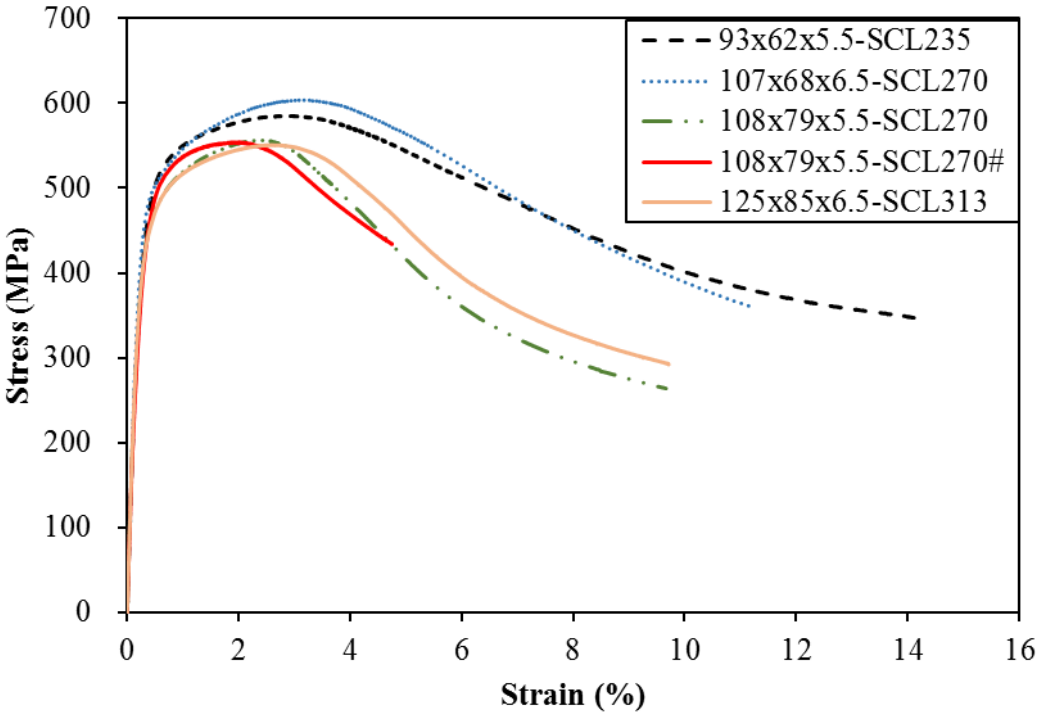

(a) Static stress-strain responses

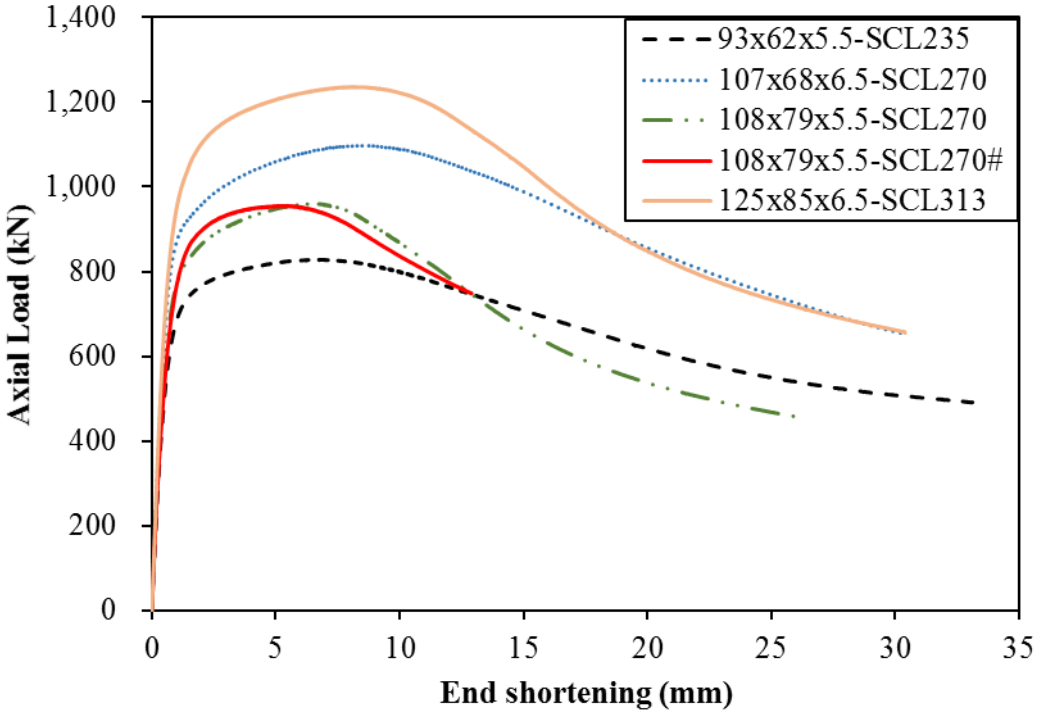

(b) Static load-end shortening histories

Figure 18. Results from fixed-ended stub column tests.

Figure 19. Failed SOHS stub column specimens

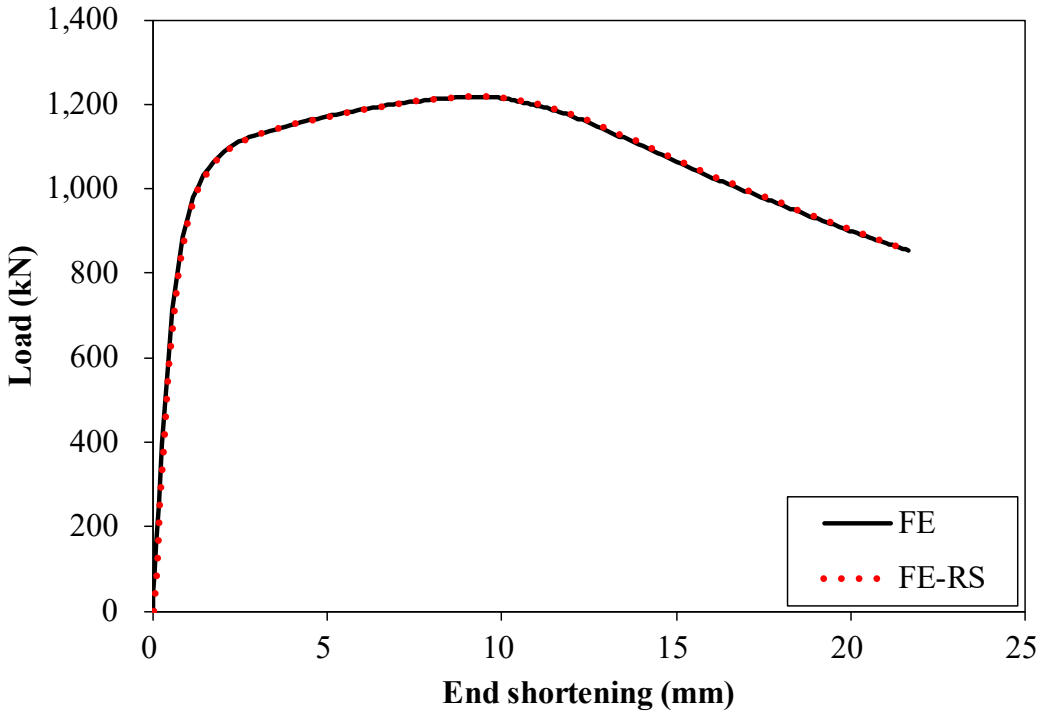

Figure 20. Comparison of FE models of SOHS stub column 125×85×6.5-SCL313 with and without explicit inclusion of residual stresses

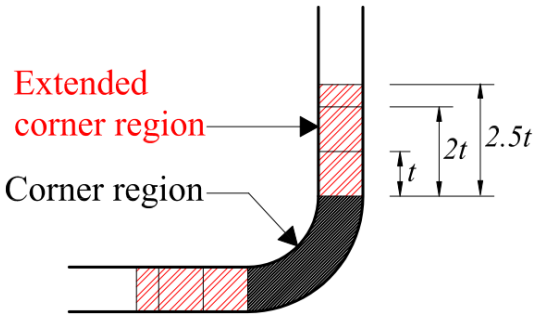

Figure 21. Extension of corner region of SOHS

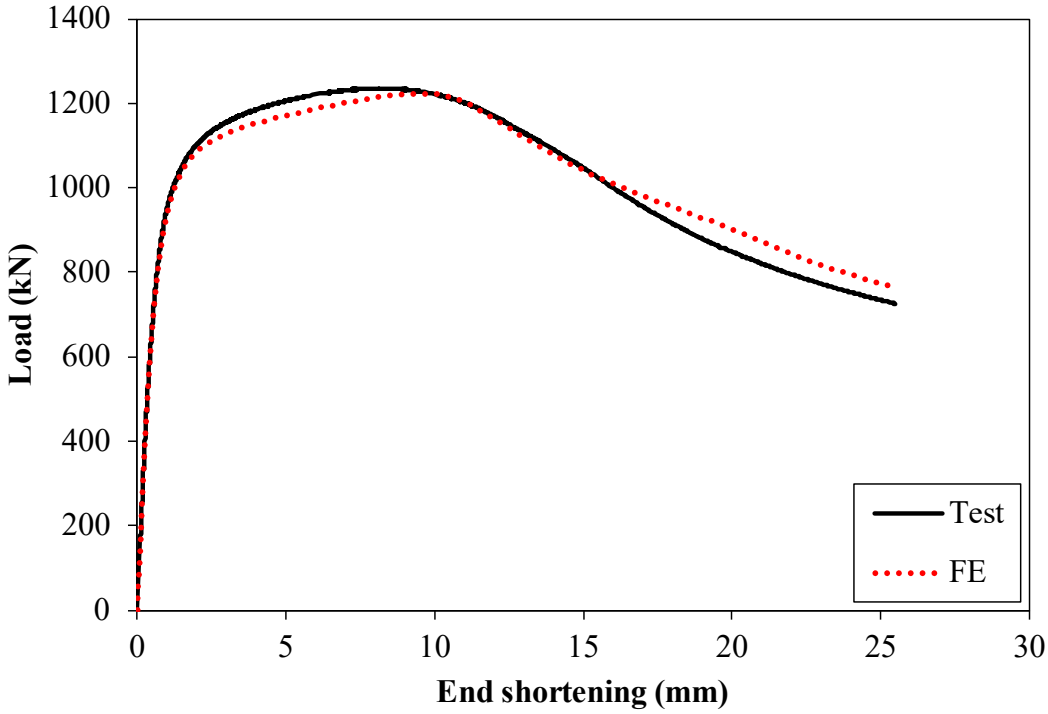

Figure 22. Experimental and numerical load-end shortening responses of SOHS stub column 125×85×6.5-SCL313

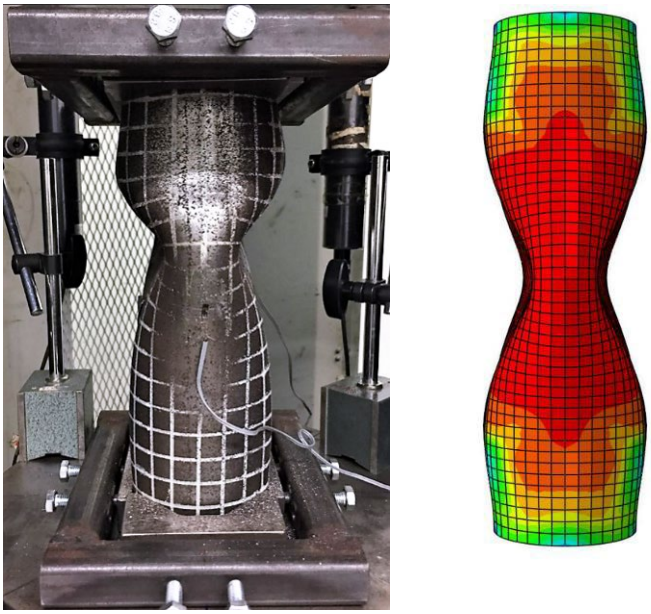

Figure 23. Comparison between experimental and numerical failure modes for SOHS stub column 125×85×6.5-SCL313

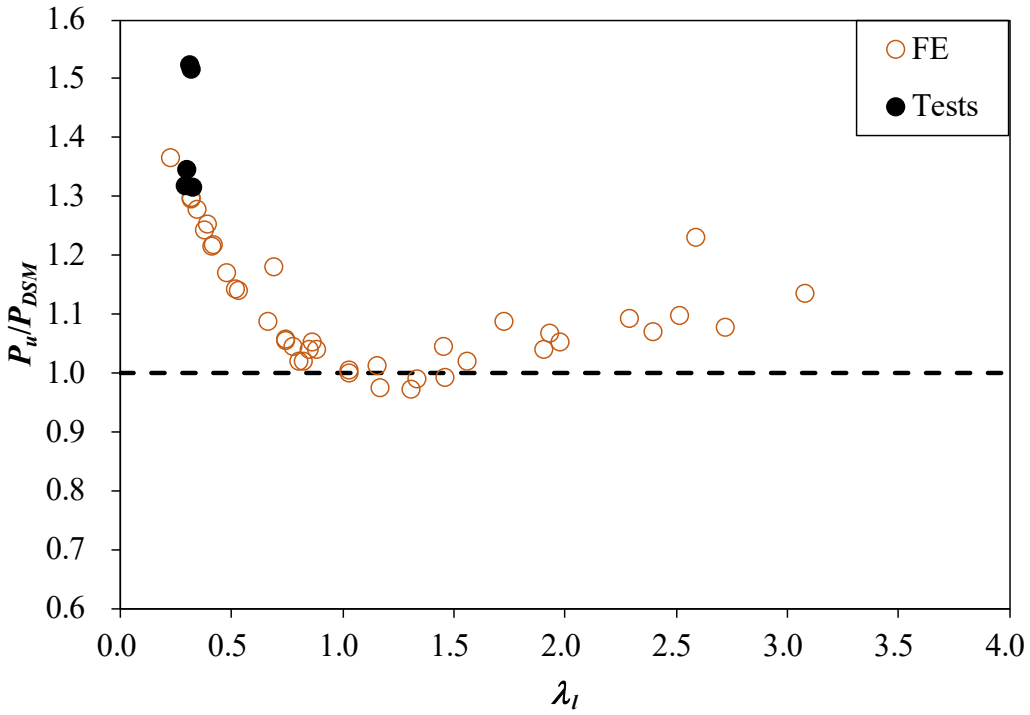

Figure 24. Comparison of test and FE results of SOHS stub columns with design strength predicted by the DSM

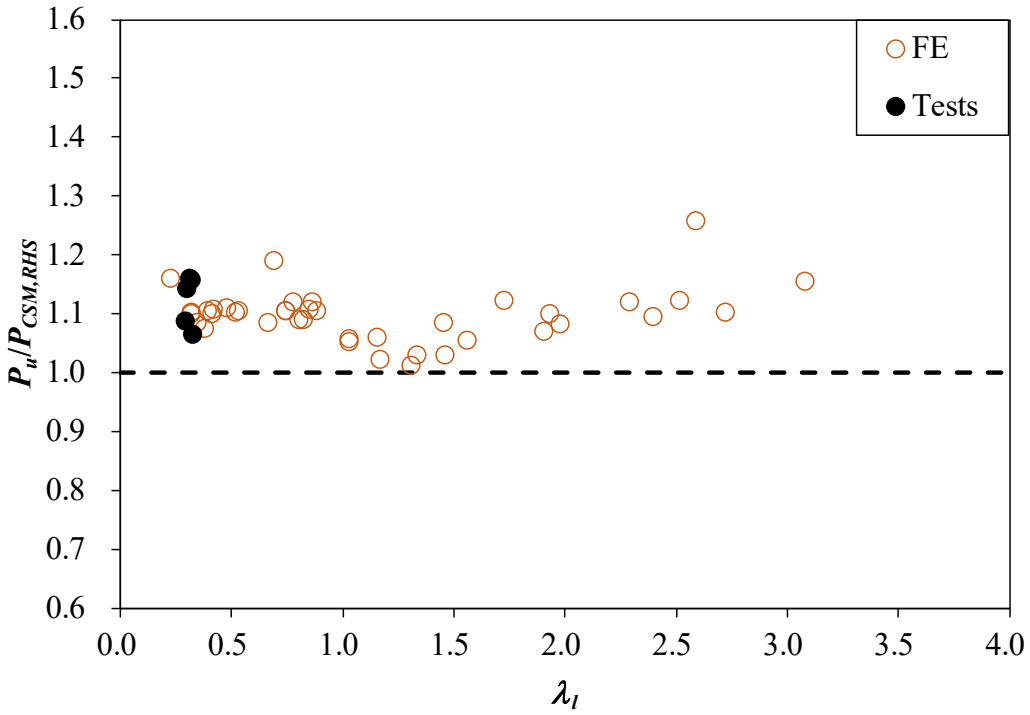

Figure 25. Comparison of test and FE results of SOHS stub columns with design strength predicted by the RHS approach of the CSM

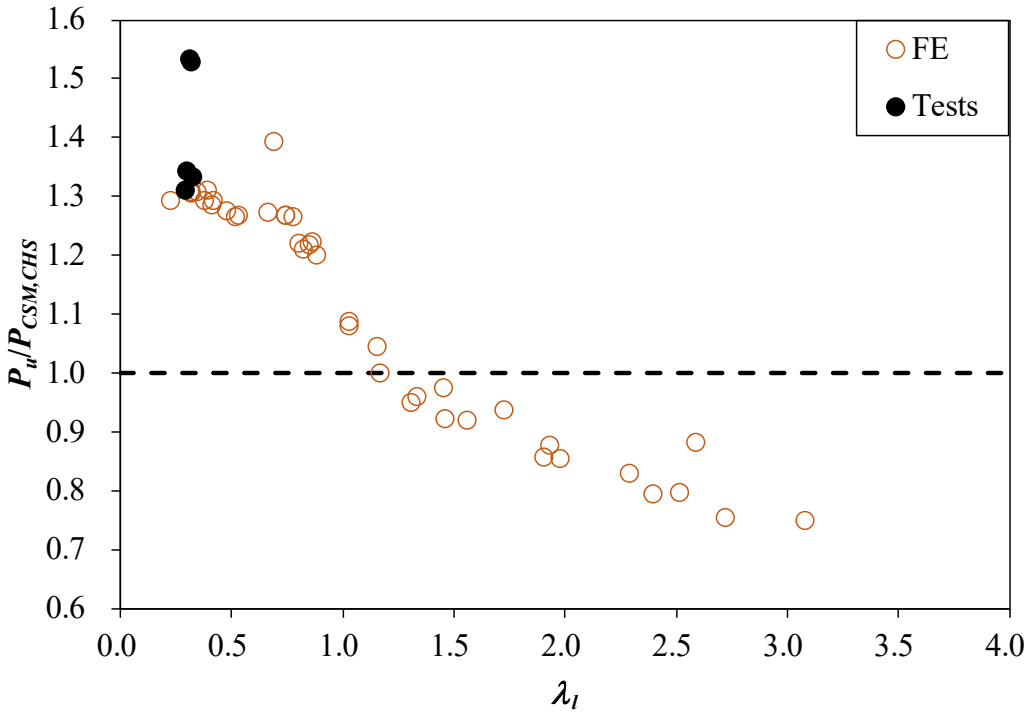

Figure 26. Comparison of test and FE results of SOHS stub columns with design strength predicted by the CHS approach of the CSM

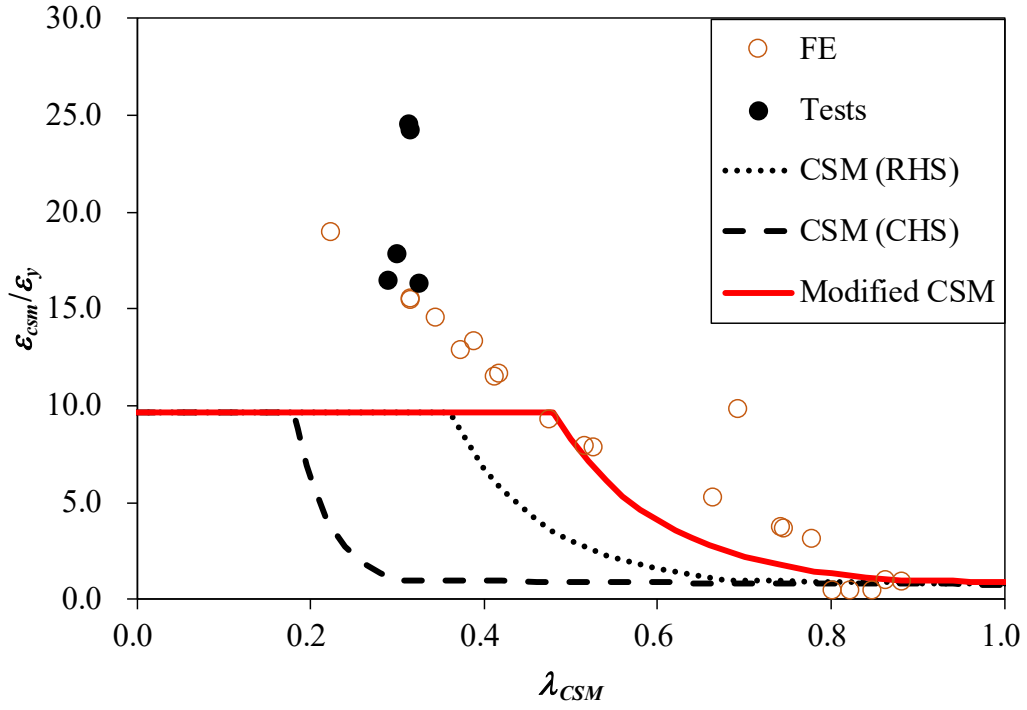

Figure 27. CSM base curves with experimental and numerical data

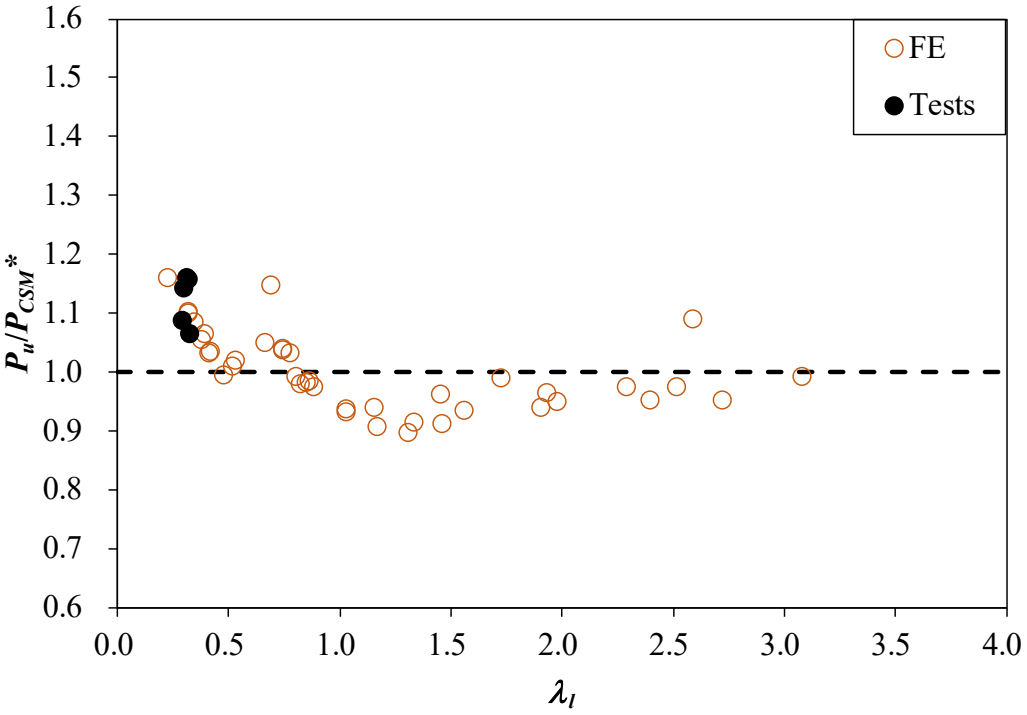

Figure 28. Comparison of test and FE results of SOHS stub columns with design strength predicted by the modified CSM

Section	Flat (TC1)				Curved (TC2)				Corner (TC3)			
	E (GPa)	$\sigma_{0.2}$ (MPa)	σ_u (MPa)	ε_f (%)	E (GPa)	$\sigma_{0.2}$ (MPa)	σ_u (MPa)	ε_f (%)	E (GPa)	$\sigma_{0.2}$ (MPa)	σ_u (MPa)	ε_f (%)
93×62×5.5	204	453	549	22	211	444	551	23	211	511	600	16
107×68×6.5	211	475	548	20	209	450	540	26	210	518	605	16
108×79×5.5	206	460	555	27	199	366	545	26	185	507	625	17
125×85×6.5	207	439	530	26	204	419	531	28	203	486	577	19

Table 1. Measured material properties of SOHS obtained from tensile coupon tests

Coupon location	E (GPa)	$\sigma_{0.2}$ (MPa)	σ_u (MPa)	ε_f (%)	Coupon location	E (GPa)	$\sigma_{0.2}$ (MPa)	σ_u (MPa)	ε_f (%)
1	204	433	529	27	10	208	450	524	25
2	202	456	554	23	11	208	474	532	24
3	202	394	591	22	12	196	397	560	20
4	198	476	585	18	13	207	394	548	24
5	209	460	531	26	14	209	419	550	27
6	204	467	529	25	15	205	374	525	29
7	213	447	523	25	16	215	379	525	31
8	206	440	527	27	17	205	415	536	30
9	210	435	518	27	18	207	409	531	30

Table 2. Measured material properties obtained from tensile coupon tests in half-section of SOHS 125×85×6.5

Specimen	D (mm)	B (mm)	t (mm)	r_o (mm)	r_i (mm)	L (mm)	ω_l Convex (mm)	ω_l Concave (mm)
93×62×5.5-SCL235	93.4	62.0	5.58	15.5	9.9	234.4	0.153	-0.205
107×68×6.5-SCL270	107.2	67.7	6.34	16.7	10.4	269.9	0.122	-0.584
108×79×5.5-SCL270	108.2	78.8	5.52	12.4	6.9	271.5	0.110	-0.250
108×79×5.5-SCL270#	108.4	79.0	5.51	12.6	7.1	271.5	0.111	-0.287
125×85×6.5-SCL313	124.7	84.8	6.45	17.2	10.7	313.0	0.205	-0.459

Table 3. Measured dimensions and local geometric imperfections of SOHS stub columns

Specimen	E_{SC} (GPa)	$\sigma_{0.2\text{-}SC}$ (MPa)	$\sigma_{u\text{-}SC}$ (MPa)	$\frac{\sigma_{0.2\text{-}SC}}{\sigma_{0.2\text{-}TC}}$	$\frac{\sigma_{u\text{-}SC}}{\sigma_{u\text{-}TC}}$
93×62×5.5-SCL235	209	486	585	1.09	1.06
107×68×6.5-SCL270	221	491	604	1.09	1.12
108×79×5.5-SCL270	214	459	556	1.25	1.02
108×79×5.5-SCL270#	210	466	554	1.27	1.02
125×85×6.5-SCL313	216	452	551	1.08	1.04

Table 4. Results obtained from the average stress-strain relationship over the complete cross-section

Specimen	P_{Exp} (kN)	δ_u (mm)	P_y^ (kN)	$\frac{P_{Exp}}{P_y}$^
93×62×5.5-SCL235	828.1	6.6	650.0	1.27
107×68×6.5-SCL270	1097.9	8.8	859.6	1.28
108×79×5.5-SCL270	959.8	6.8	741.0	1.30
108×79×5.5-SCL270#	955.7	5.5	740.8	1.29
125×85×6.5-SCL313	1235.8	8.1	982.1	1.26

^Considering the cold-forming enhancement.

Table 5. SOHS stub column test results

Specimen	P_{Exp}/P_{FE} Corner extension			P_{Exp}/P_{FE} Local imperfection		
	t	$2t$	$2.5t$	$t/16$	$t/50$	$t/100$
93×62×5.5-SCL235	1.01	1.00	1.00	1.04	**1.00**	1.01
107×68×6.5-SCL270	1.04	1.03	1.03	1.07	**1.03**	1.03
108×79×5.5-SCL270	0.99	0.98	0.97	1.02	**0.98**	0.97
108×79×5.5-SCL270#	0.98	0.97	0.97	1.01	**0.97**	0.97
125×85×6.5-SCL313	1.03	1.02	1.01	1.06	**1.01**	1.01
Mean	1.01	1.00	1.00	1.04	**1.00**	1.00
COV	0.023	0.024	0.024	0.024	**0.023**	0.025

Table 6. Summary of sensitivity study of SOHS stub columns

Specimen	P_{FE} (kN)	Specimen	P_{FE} (kN)
450×360×20-SCL1125	15304.1	350×200×2.5-SCL875	584.5
450×360×10-SCL1125	6627.1	300×240×6-SCL750	2511.0
450×360×3-SCL1125	1045.6	245×140×4-SCL612.5	1039.6
450×300×16-SCL1125	10823.4	240×160×6-SCL600	2051.4
450×300×10-SCL1125	6251.8	240×160×3-SCL600	666.6
450×300×3-SCL1125	899.1	240×160×2-SCL600	372.7
450×225×20-SCL1125	12532.3	200×160×16-SCL500	5566.9
450×225×4-SCL1125	1253.3	200×160×3-SCL500	671.5
450×225×3-SCL1125	813.0	200×160×2-SCL500	365.4
450×200×16-SCL1125	9277.7	180×120×10-SCL450	2889.2
450×200×10-SCL1125	5219.1	180×120×3.5-SCL450	819.8
450×200×2.5-SCL1125	584.8	180×120×2-SCL450	315.3
450×180×16-SCL1125	9004.2	180×80×8-SCL450	1939.6
450×180×10-SCL1125	4998.8	180×80×2-SCL450	272.8
450×180×5.5-SCL1125	1969.4	150×75×8-SCL375	1722.9
450×180×4-SCL1125	1165.0	150×75×2.5-SCL375	378.8
420×240×20-SCL1050	12412.8	150×60×6-SCL375	1153.8
420×240×8-SCL1050	4058.2	150×60×2-SCL375	239.2
420×240×2.5-SCL1050	610.5	140×80×8-SCL350	1692.5
350×200×8-SCL875	3694.5	140×80×2-SCL350	265.7

Table 7. Parametric study on cold-formed steel SOHS stub columns

Number of specimen		$\frac{P_u}{P_{DSM}}$	$\frac{P_u}{P_{CSM,RHS}}$	$\frac{P_u}{P_{CSM,CHS}}$	$\frac{P_u}{P_{CSM}}$ *
Test:5	FE:40				
	Mean	1.14	1.10	1.14	**1.01**
	COV	0.123	0.040	0.189	**0.073**
	ϕ	0.85	1.00	1.00	**0.85**
	β	2.99	2.37	1.96	**2.61**

*Modified design method.

Table 8. Comparison of SOHS stub column test and FE results with predicted strengths